Volume Title
ASP Conference Series, Vol. **Volume Number**
Author

NIRIS - the Second Generation Near-Infrared Imaging Spectro-polarimeter for the 1.6 Meter New Solar Telescope

W. Cao,[1,2] P. R. Goode,[1,2] K. Ahn,[2] N. Gorceix,[2] W. Schmidt,[3] and H. Lin[4]

[1]*New Jersey Institute of Technology, Center for Solar-Terrestrial Research, 323 Martin Luther King Blvd., Newark, NJ 07102, U.S.A.*

[2]*Big Bear Solar Observatory, 40386 North Shore Lane, Big Bear City, CA 92314, U.S.A.*

[3]*Kiepenheuer-Institut für Sonnenphysik, Schöneckstr. 6, D-79104 Freiburg, Germany*

[4]*Institute for Astronomy, University of Hawaii, 34 Ohia Ku Street, Pukalani, Maui, HI 96768, U.S.A.*

Abstract. The largest aperture solar telescope, the 1.6 m New Solar Telescope (NST) has been installed at the Big Bear Solar Observatory (BBSO). To take full advantage of the NST's greatest potential, we are upgrading the routinely operational InfraRed Imaging Magnetograph (IRIM) to its second generation, the NIRIS (Near-InfraRed Imaging Spectropolarimeter). NIRIS will offer unprecedented high resolution spectroscopic and polarimetric imaging data of the solar atmosphere from the deepest photosphere through the base of the corona. With the aid of the BBSO adaptive optics (AO) system, the spatial resolution will be close to the diffraction limit of the NST. The spectroscopic cadence will reach one second, while polarimetric measurements, including *Stokes I*, *Q*, *U*, *V* profiles, remain at a better than 10 s cadence. Polarization sensitivity is expected to be reach $\sim 10^{-4} I_c$. NIRIS will cover a broad spectral range from 1.0 to 1.7 μm, with particular attention to two unique spectral lines: the Fe I 1565 nm doublet has already proven to be the most sensitive to Zeeman effect for probing the magnetic field in the deepest photosphere; the He I 1083 nm multiplet is one of the best currently available diagnostic of upper chromospheric magnetic fields that allows one to map the vector field at the base of the corona. NIRIS will be built on dual Fabry-Pérot Interferometers (FPIs), each of which has an aperture of 100 mm. The larger aperture of FPIs allows the available field-of-view up to one and half minutes with a spectral power of $\sim 10^5$.

1. Introduction

InfraRed Imaging Magnetograph (IRIM) is the first generation near-infrared imaging spectro-polarimeter of the Big Bear Solar Observatory (BBSO), which was successfully developed for BBSO's now-retired 0.6 m telescope (Cao et al. 2006). Based on a 2.5 nm interference filter, a unique 0.25 nm birefringent Lyot filter, and a single Fabry-Pérot Interferometer (FPI), IRIM is capable of providing a bandpass as low as $\sim$ 0.01 nm in a telecentric configuration. IRIM has been re-designed and tailored to the New Solar Telescope (NST), serving as a testbed for next generation instrumenta-

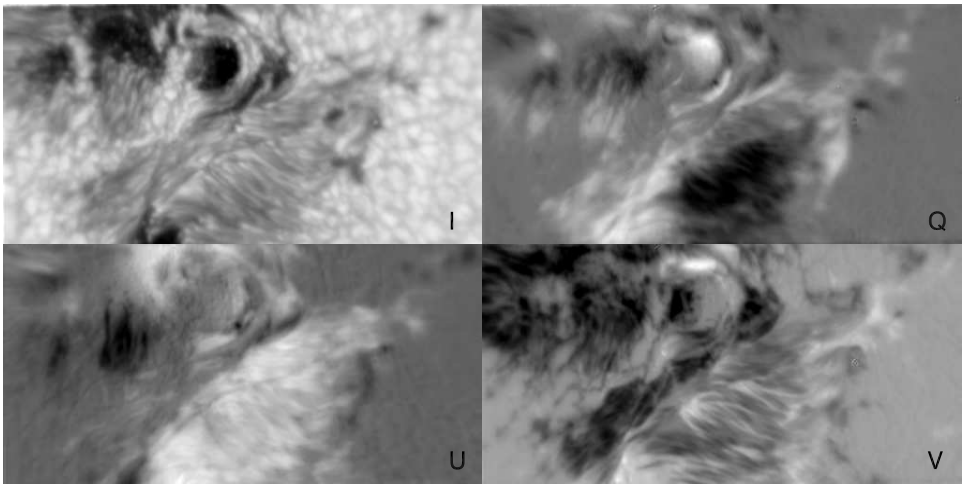

Figure 1. Calibrated IRIM vector magnetogram without any image reconstruction near AR 11283 at 463W 119N, taken on 7 Sept. 2011. Stokes *I* and *V* are sliced in the blue wing of the Fe I 1564.85 nm line while *Q* and *U* are sliced in the line center. Dual-beam technology was employed to minimize seeing-induced noise. The field of view of IRIM is about 50″×25″.

tion development. In 2010 Summer, IRIM was temporarily installed on the horizontal optical bench in BBSO's Coudé Lab, and thereafter revealed its capabilities in high spatial resolution vector magnetic fields probing (as shown in Figure 1). Unfortunately, the IRIM is unable to fully take advantage of the NST with AO for the following reasons: (1) low transmission: high transmission of a narrow-band instrument enables short exposures, which are particularly critical to high cadence, high spatial polarimetric observations. Modern coating technologies enable FPIs and interference filters to have a peak transmission of up to 90%. However, IRIM's Lyot filter has a comparatively low transmission of about 15%. Total system transmission is about a factor of five less than that of a dual Fabry-Pérot system. Low system throughput leads to a typical exposure time of 180 ms, which is too long to freeze atmospheric turbulence for high resolution polarimetry and post-processing image reconstruction. (2) narrow wavelength coverage: a recent NIR survey has discovered a large number of candidate spectral lines between 1.0 and 1.7 μm. Among them, the Fe I 1564.8 nm with a $g = 3$ Landé factor represents the most magnetically sensitive spectral line formed in the low photosphere. The He I 1083.0 nm is probably the spectral line with the best potential diagnostic capabilities for magnetism in the upper chromosphere. Unfortunately, IRIM is only capable of having its passband tuned in a range of ±10 nm around 1565 nm. The main reason derives from the narrow achromatic range of the NIR waveplates in the Lyot filter. (3) small FOV: according to the Lagrange optical invariant, the available FOV is determined by telescope aperture, instrument aperture, and f-number (f#). IRIM's FPI has a clear aperture of 70 mm which defines a square FOV of 50″. A dual beam polarimetry further reduce the FOV to 50″ × 25″, which is not sufficient for probing solar flares since they can occur "unannounced" anywhere in the extended FOV. Therefore, upgrading of the IRIM to its second generation is not only essential but also urgent.

Table 1. NIRIS baseline characteristics

Wavelength range	1000 ~ 1700 nm
Spectral resolving power	$\lambda/\Delta\lambda = 1.0 \sim 1.5 \times 10^5$
FOV	85″
Parasitic light	$< 10^{-3}$
Spatial sampling	$0\farcs083 \times 0\farcs083$ pixel^{-1}
Exposure time	20 ms for S/N≥125
Strehl ratio	≥ 0.7
Zeeman sensitivity	$\sim 10^{-4} I_c$
Spectroscopy	< 1 s cadence
Vector spectro-polarimetry	< 10 s cadence

2. NIRIS Development Strategy and Expected Performance

NIRIS, the Near-Infrared Imaging Spectro-polarimeter is the second generation instrument which is being developed for the 1.6 m clear aperture NST. In a detailed, careful study, we have arrived at the baseline design for NIRIS. Table 1 lists some of the preliminary instrumental characteristics. The conceptual design of the NIRIS is quite straightforward. In tandem, two NIR Fabry-Pérot etalons with apertures of 100 mm are set up in a telecentric configuration – effectively reducing spectral inhomogeneity over the FOV. In a telecentric configuration, the FPIs are placed near a focus of the solar image, where the entrance pupil of telescope is at infinity. Two narrow-band interference filters, each transmitting in a region around 1083 nm and 1565 nm, will isolate the central transmission and ensure that the parasitic light is kept below 0.1%. NIRIS will provide four operating modes: polarimetric mode (full spectral profile with polarization optics), spectroscopic mode (full spectral profile without polarization optics), Doppler mode (a few selected spectral points), and photometric mode (single spectral point). In the polarimetric mode, a dual-beam design will be adopted to reduce polarization crosstalk induced by seeing.

2.1. Optical Design of the NIRIS

Figure 2 schematically depicts the NIRIS layout. The primary path of the solar beam is shown in orange. At the AO output, a real solar image with an $f\#$ of 20 is fed to the science instruments. A dichroic filter separates the NIR and visible light, respectively.

NIRIS will employ a telecentric configuration. The NST entrance pupil is imaged by L1 on the pupil plane and is then collimated by L2 through the dual FP etalons. However, the solar image is collimated by L1 and an intermediate image is formed again by L2 between the two etalons. Since every image point has the same incident angle entering the etalons, this configuration enables an invariance of the passband across the field of view regardless of any cavity error. Then, the intermediate image is re-imaged onto the IR focal plane array (IRFPA1) by L3 and L4, where the pupil is at infinity. For a purely telecentric configuration, the passband of a FPI is associated with its effective FWHM and the maximum angle of the incident beam. According to the Lagrange optical invariant, this maximum angle depends on the FOV and the aperture ratio of the telescope and FPI. To achieve sufficient spectral power with the specifications in Table 1, the beam should have an $f\#$ of 145 after L2 and the round FOV will

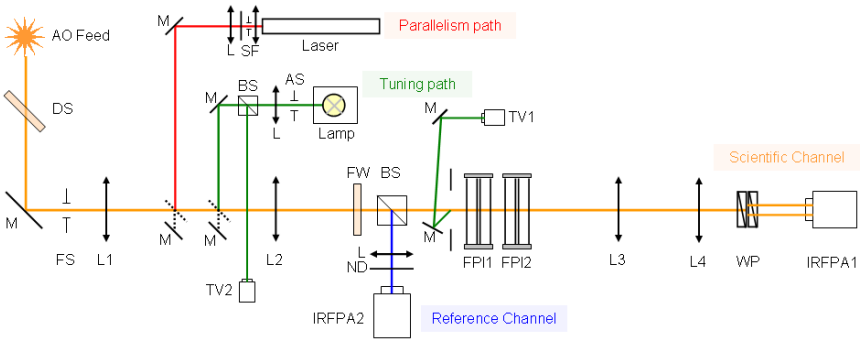

Figure 2. Schematic drawing of the NIRIS layout. The orange line represents the principal optical path, while the polarization modulator is not shown here. The secondary paths are also indicated. The meaning of the labels is as follows: AS: aperture stop; BS: beamsplitter; DS: dichroic; FPI: Fabry-Pérot interferometer; FS: field stop; IRFPA: infrared focal plane array; L: lens; M: mirror; ND: neutral density filter; SF: spatial filter; TV: TV camera; WP: Wollaston prism.

be about 85″. In order to minimize so-called spurious polarization signals from seeing-induced intensity variations, two Wollaston prisms will be employed to simultaneously produce two orthogonal, linearly polarized beams on IRFPA1. To deliver optimal optical performance, most of the optical components in the NIRIS relay path will have to be custom-designed and manufactured. We have completed preliminary Zemax optical design for the NIRIS primary path. Spot diagrams show diffraction limited image quality in dual beam at 1083.0 nm and 1565.0 nm.

A series of secondary optical paths, shown with green, red and blue lines in Figure 2, will play additional important roles in system alignment and calibration. These auxiliary channels include: (1) A parallelism path, using a He-Ne NIR laser for the proper parallelism of two FPIs plates; (2) A tuning path: using a broad-band lamp to accurately align the transmission profiles of the two FPIs; (3) A reference channel: to obtain broad-band images simultaneously with the narrow-band images as a reference for the instantaneous atmospheric distortions or transmission fluctuations. IRIM NIR camera will be used for this channel.

2.2. Fabry-Pérot Interferometers

FPIs are at the core of the NIRIS project. We considered and selected their specifications very carefully to meet all requirements to optimize scientific research. Table 2 lists the baseline characteristics of FPIs and prefilters. Many characteristic parameters need to be compromised, as discussed below.

(1) Wavelength coverage and coating: we have received theoretical data from one FPI vendor, IC Optical Systems for the first FPI that is currently being purchased. Figure 3 shows two designs, and the opinion of the coating designer is that the 1000-1700 nm is the sensible maximum range. They would use standard techniques and pre-coating calibration to manufacture the coating. Calculated coating reflectivity is 95% with a variation less that ±0.5% over the full operating range.

(2) Spectral power, FOV and FPI aperture: optical design obeys the Helmholtz-Lagrange invariant, which defines the relation among the $f\#$, FOV, FPI aperture and telescope diameter. In a telecentric mount, spectral power and image quality (von der

Table 2. FPIs and prefilters baseline characteristics.

FPI Manufacture	IC Optical Systems
Aperture	100 mm
Reflectivity	95%±0.5%
Absorption coefficient	0.2%
Cavity spacings	FPI1: 2226.0 μm
	FPI2: 615.7 μm
Scaning range	4.1 μm
Flatness before coating	$\lambda/200$
Controller	CS-100
Prefilter Manufacture	Barr Associates, Inc.
Aperture	25.4 mm
Cavities	3 or 4
FWHM	0.8-1.5 nm
Central wavelengths	1083 nm, 1565 nm

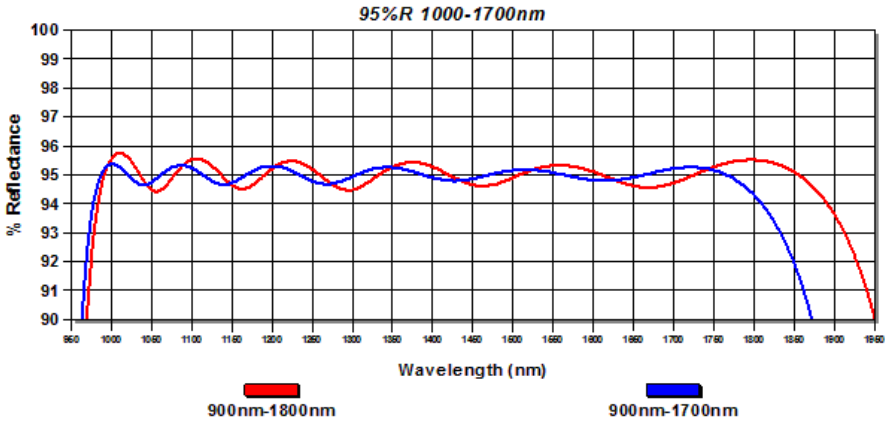

Figure 3. Simulated reflectance curves of FPI coating provided by manufacturer, covering 1000 nm-1800 nm or 1000 nm-1700 nm.

Lühe & Kentischer 2000) benefit by increasing the $f\#$ of the incident beam. We simulated two extreme cases at 1083 nm and 1565 nm and plot the NIRIS spectral power as a function of FPI aperture and FOV, as shown in Figure 4. Given a baseline of 1.0×10^4 spectral power, we selected FPIs that have 100 mm aperture, and FOV to be 85″.

(3) Cavity spacing ratio and parasitic light: parasitic light is the additional flux from the sidelobes of the spectral transmission profiles. For a given prefilter, an optimal selection of the cavity spacing ratio between the FPIs can tremendously minimize the parasitic light. Assuming that the two FPIs have same the reflectivity (95%) and absorption coefficient (0.2%), the transmission profiles of FPI1 and FPI2 are plotted in the top panel of Figure 5. Given a 2-cavity prefilter with a FWHM of 1.5 nm, which is shown as a dashed line, the resulting transmission profile shows a single transparency peak at 1564.8 nm, as well as a number of low transparency sidelobes. Based on the resulting transmission profile, the parasitic light is calculated as a function of the cavity spacing ratios, which are shown in the middle panel and bottom panel of Figure 5.

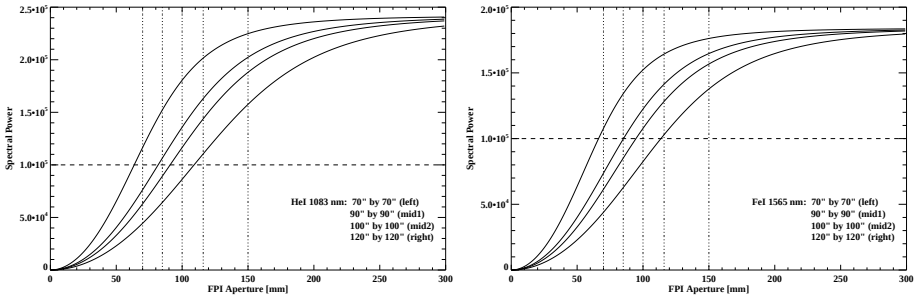

Figure 4. Spectral power as a function of FPI aperture and FOV in a telecentric configuration.

The dotted line indicates the best ratio between the two FPIs, which is equal to 0.2766. Therefore, default cavity spacings of the two FPIs are 2226.0 and 615.7 μm, respectively. Also, we performed similar simulations for the spectral lines of He I 1083 nm.

2.3. Polarimeter

The NIRIS polarimeter will heavily leverage the design and hardware of the IRIM polarimeter. The optical design, calibration procedure and implementation of the IRIM polarimeter have been discussed in detail by Goode et al. (2011) and Cao et al. (2011).

The modulator is a zero-order waveplate with a retardation of $0.3525\lambda \pm \lambda/350$ at 1564.85 nm. It was fabricated by sandwiching a birefringent polymer between a pair of BK7 grade A fine annealed glass elements. The modulator is rotated continuously with its rotation integrated to the frame rate of the IR camera. A frame will be acquired while the plate rotates from 0° to 22.5° and then from 22.5° to 45°, and so on. One rotation of the plate will result in the acquisition of 16 frames.

To minimize seeing-induced spurious polarization, two new Wollaston prisms are designed as the analyzers to offer a dual-beam for differential polarimetry for NIRIS. The first one acts as a polarizing beam splitter, while the second makes the beam parallel. New Wollaston prism has a physical size of 50 mm $\times$ 50 mm. It is a combination of two calcite sheets, each having its fast axis orthogonal to the other. The surface between the two sheets is wedged by 8°.

Much effort has been made to improve the cadence and synchronization between the rotating waveplate and image acquisition by the camera. The total transmission of the NIRIS is about a factor of 6 larger than that of the IRIM. The substantial increase in NIR photons flux will enable us to increase the rotation rate to up to 3 revolution/s. In this case, we need an IR camera working at a frame rate of at least 48 frames/s. The current IRIM camera can only operate at 10 frames/s for acquiring scientific data with sufficiently low noise. In one revolution, the control computer transfers data of 1st-16th frames from the framegrabber to the computer memory. Meanwhile, it commands the FPIs to shift wavelength to the next scanning point. These two tasks have to be completed within one frame's timing. Therefore, the 17th frame must be discarded. From the 18th frame, the next burst begins for another 16 frames. This procedure is repeated until it finishes all spectral tuning with, typically, 13 wavelength points. So, NIRIS spectro-polarimetry cadence will be typically 10 s. After a series of post-processing including dark and flat field corrections, rectifying spectra, removal of the instrument profile, and polarimetric calibration, etc., the polarimetry data are then input to the

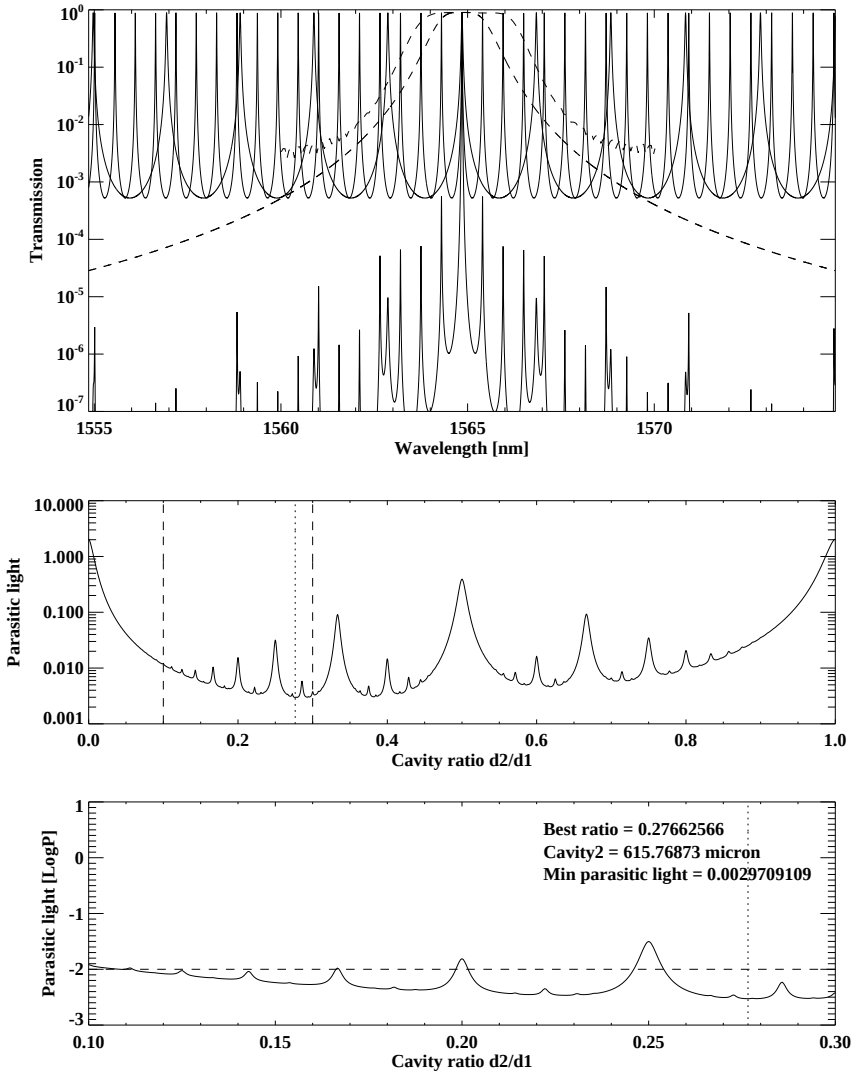

Figure 5. *Top*: Transmission curves of FPI1 and FPI2 with 95% reflectivity and 0.2% absorption coefficient. Dashed lines plot the transmission profiles of two 2-cavity prefilters with fwhm of 1.5 nm and 2.5 nm. *Middle*: Parasitic light *vs.* ratio for dual FPIs in a telecentric mount. The two vertical dashed lines define a range where the deepest minima can be found. *Bottom*: Parasitic light *vs.* ratio within the range defined in the *middle panel*.

Stokes inversion code for inferring maps of vector field strengths. A majority of hardware and calibration elements at 1565 nm can be utilized by the NIRIS. At this moment, we are still debating between two modulator designs: (1) two individual waveplates at 1083.0 nm and 1565.0 nm; (2) a single achromatic waveplate over the NIR wavelength range. We will actively seek the vendor who is able to produce waveplate at 1083 nm, or achromatic waveplate.

Table 3. Teledyne H2RG NIR camera performance.

Parameter	Specification
Readout integrated circuit	HAWAII-2RG
Detector material	HgCdTe
FPA format	2048×2048
Pixel size	$18\ \mu\text{m} \times 18\ \mu\text{m}$
Cutoff wavelength	$2.5\ \mu\text{m}$
Quantum Efficiency	$\geq 80\%$
Well capacity	150,000 e^-
Outputs	Programmable 1, 4, 32
Readout noise	$\leq 70e^-$
Frame rate	≤ 70 Hz
Interface	CamLink LVDS
Cooling system	LN_2

2.4. NIR detector

Until recently, the only NIR FPA camera available at BBSO was a 1024×1024 HgCdTe TCM8600 CMOS camera (Cao et al. 2005), manufactured by the Rockwell Scientific Company (RSC, now Teledyne Imaging Sensors) in 2002. In order to satisfy the diverse observational requirements from the NST, this camera was repackaged and upgraded (Cao et al. 2010) at Infrared Laboratories Inc. in the beginning of 2010. A new ND-5 dewar was designed to house the TCM8600 array with a low background filter wheel, inverted operation and at least 12 hours of hold time between fills. Even so, its characteristics are quite insufficient to meet the requirements from the NIRIS for the following reasons: (1) small FPA format: NIRIS aims at diffraction limited observations. The Rayleigh diffraction limit of NST, $\theta \simeq \lambda/D$ is $0\farcs17$ at 1083 nm. Nyquist frequency defines the maximum spatial sampling of $0.083''$ pixel^{-1}. NIRIS employs a dual beam for polarimetry measurement to minimize seeing-induced polarization crosstalk. Thus, a 1K×1K FPA can only accommodate a FOV of $85'' \times 42.5''$. Such a FOV is not sufficient for observations of flare, a middle size sunspot or active regions, which typically require a FOV of 1-2 arcmin. (2) slow readout: calculations of the photon budget show that NIRIS is able to reduce exposures shorter than 20 msec and still achieve Poisson-limited S/N ratios of better than 125:1. The substantial photon flux allows us to increase the rotation rate of the modulator to up to 3 revolution/s with good S/N. In this case, we need a camera that can provide a frame rate of at least 48 frame/s. We have also noticed the ever increasing noise of the IRIM camera along with its aging over the past few years. High noise level tremendously limits the application of the speckle reconstruction algorithm. Although the IRIM camera has a nominal frame rate of 30 Hz, its real operation must be lower than 15 Hz to avoid too much noise. (3) dark pattern: the moveable dark patterns are a newly-found problem (Cao et al. 2010). As the integration time increases, two dark patterns sweep across FPA bi-directionally toward the detector center. The positions of the dark patterns depend strictly on the adopted integration time. Although the two dark patterns are able to be corrected with flat fields, the flat fields must have exactly the same integration time as image exposures.

Teledyne Imaging Sensors has developed the next generation NIR camera system based on the H2RG FPA and SIDECAR ASIC focal plane electronics. This H2RG NIR

camera is particularly suitable for the NIRIS detector system with a good performance over its large format, fast readout, high quantum efficiency and low noise. Table 3 lists the H2RG NIR camera performance properties. Dual beam polarimetry with the NIRIS only requires a real region of 1k×2k on the FPA. We will use ROI (region of interest) readout to balance fast readout and low noise. In addition, H2RG has exactly the same pixel size as BBSO's 1k×1k IRIM camera, allowing us to easily transfer this camera to the NIRIS reference channel with the same FOV and image scale. The reference channel will obtain NIR broad-band images simultaneously with the narrow-band images as a reference for the instantaneous atmospheric distortions or transmission fluctuations.

3. Summary

In astronomy new spectral windows opened by new hardware always usher in new eras of discovery, and that time has come for the solar infrared. Meanwhile, the NST's success opens a door to unprecedented high resolution observations. Its 2.0 m^2 aperture of the primary mirror also provides a huge "light-bucket" to accumulate sufficient photons for high temporal cadence observations in the visible and NIR.

NIRIS will be one of the first imaging spectro-polarimeter working in the NIR, which will enable the NST to provide the community the highest cadence, diffraction limited spectroscopic and polarimetric data over a large FOV from the deepest photosphere through the base of corona. Benefitting from the largest aperture solar telescope in operation, the NST, BBSO's unique seeing conditions, and the state-of-the-art AO system, the NIRIS will enable the greatest potential for breakthrough discoveries in probing the fundamental character of our dynamic star and the origin of space weather.

Acknowledgments. We gratefully acknowledge the support of NSF (AGS-084712 6 and AGS-0745744), NASA (NNX08BA22G) and AFOSR (FA9550-09-1-0655).

References

Cao, W., Ahn, K., Goode, P. R., Shumko, S., Gorceix, N., & Coulter, R. 2011, in Solar Polarization 6, edited by J. R. Kuhn, D. M. Harrington, H. Lin, S. V. Berdyugina, J. Trujillo-Bueno, S. L. Keil, & T. Rimmele, vol. 437 of Astronomical Society of the Pacific Conference Series, 345

Cao, W., Coulter, R., Gorceix, N., & Goode, P. R. 2010, in Society of Photo-Optical Instrumentation Engineers (SPIE) Conference Series, vol. 7742 of Society of Photo-Optical Instrumentation Engineers (SPIE) Conference Series

Cao, W., Jing, J., Ma, J., Xu, Y., Wang, H., & Goode, P. R. 2006, PASP, 118, 838

Cao, W., Xu, Y., Denker, C., & Wang, H. 2005, in Society of Photo-Optical Instrumentation Engineers (SPIE) Conference Series, edited by R. E. Longshore, vol. 5881 of Society of Photo-Optical Instrumentation Engineers (SPIE) Conference Series, 245

Goode, P. R., Cao, W., Ahn, K., Gorceix, N., & Coulter, R. 2011, in Solar Polarization 6, edited by J. R. Kuhn, D. M. Harrington, H. Lin, S. V. Berdyugina, J. Trujillo-Bueno, S. L. Keil, & T. Rimmele, vol. 437 of Astronomical Society of the Pacific Conference Series, 341

von der Lühe, O., & Kentischer, T. J. 2000, A&AS, 146, 499